

ANGULAR MOMENTUM EVOLUTION OF STELLAR DISKS AT HIGH REDSHIFTS

TAKU OKAMURA¹, KAZUHIRO SHIMASAKU^{1,2}, AND RYOTA KAWAMATA¹

Draft version August 31, 2018

ABSTRACT

The stellar disk size of a galaxy depends on the ratio of the disk stellar mass to the halo mass, $m_\star \equiv M_\star/M_{\text{dh}}$, and the fraction of the dark halo angular momentum transferred to the stellar disk, $j_\star \equiv J_\star/J_{\text{dh}}$. Since m_\star and j_\star are determined by many star-formation related processes, measuring j_\star and m_\star at various redshifts is essential to understand the formation history of disk galaxies. We use the 3D-HST GOODS-S, COSMOS, and AEGIS imaging data and photo- z catalog to examine j_\star and m_\star for star-forming galaxies at $z \sim 2, 3$, and 4, when disks are actively forming. We find that the j_\star/m_\star ratio is $\simeq 0.77 \pm 0.06$ for all three redshifts over the entire mass range examined, $8 \times 10^{10} < M_{\text{dh}}/h^{-1}M_\odot < 2 \times 10^{12}$, with a possible ($< 30\%$) decrease with mass. This high ratio is close to those of local disk galaxies, descendants of our galaxies in terms of M_{dh} growth, implying a nearly constant j_\star/m_\star over past 12 Gyr. These results are remarkable because mechanisms controlling angular momentum transfer to disks such as inflows and feedbacks depend on both cosmic time and halo mass and indeed theoretical studies tend to predict j_\star/m_\star changing with redshift and mass. It is found that recent theoretical galaxy formation simulations predict smaller j_\star/m_\star than our values. We also find that a significant fraction of our galaxies appears to be unstable against bar formation.

Keywords: galaxies: evolution — galaxies: high-redshift — galaxies: structure — galaxies: formation

1. INTRODUCTION

Within the Λ CDM paradigm, galaxies form in the center of hierarchically growing dark matter halos (Fall & Efstathiou 1980). In the tidal torque theory, gases and dark matter halos acquire angular momentum with log-normal distributions of the spin parameter through tidal gravitational fields (Peebles 1969). The dimensionless spin parameter is given by

$$\lambda \equiv \frac{J|E|^{1/2}}{GM^{5/2}}, \quad (1)$$

where J , E , and M are the total angular momentum, total energy, and total mass of the system. Since gases and halos share initial tidal torque fields, it is expected that gases and dark matter halos have the same amount of specific angular momentum. Gases gradually radiate away the thermal energy and then cool and collapse toward the center of dark matter halos. Their angular momentum halts the collapse and leads to a rotationally supported disk galaxy (Fall & Efstathiou 1980; White & Frenk 1991; Mo et al. 1998).

In this formation scenario of disk galaxies, the disk size of a galaxy (r_d) is given by

$$r_d = \frac{1.678}{\sqrt{2}} \left(\frac{j_d}{m_d} \right) \lambda r_{200} f_c(c_{\text{vir}})^{-1/2} f_R(\lambda, c_{\text{vir}}, m_d, j_d), \quad (2)$$

(Mo et al. 1998). Here j_d/m_d ($j_d \equiv J_d/J_{\text{dh}}$, $m_d \equiv M_d/M_{\text{dh}}$; d :star+gas) is the angular momentum retention factor and displays how much angular momentum

acquired via tidal torques is conserved during the disk formation, r_{200} is the radius of the dark matter halo within which encloses 200 times critical density, and f_c and f_R show, respectively, the difference in the density profile from an exponential profile and the gravitational effect of the disk. By assuming that the angular momentum of a disk is fully conserved, $j_d/m_d = 1$, this model successfully reproduces scaling relations of local disk galaxies: the stellar mass-size relation and the stellar mass-size scatter relation (Mo et al. 1998; Dutton & van den Bosch 2012; Romanowsky & Fall 2012). Because of the success of this picture, this model has been adopted in many semi-analytical models (e.g. Somerville et al. 2008; Porter et al. 2014; Croton et al. 2016).

However, the assumption that j_d/m_d equals to unity independent of mass and cosmic time is not trivial, because highly-complex baryonic processes such as cooling, dynamical friction, and various feedback processes can change the specific angular momentum of disk galaxies. These processes are closely dependent on the mass of host dark matter halos. For example, the mass of dark matter halos controls how much expelled gases, which exchange the angular momentum with hot halo gases, can return to the galaxies again. The accumulation of such processes may increase or decrease the disk specific angular momentum. This is why the information of angular momentum is essential for comprehensive understanding of galaxy formation and evolution. It is important to understand the evolution of the angular momentum of galaxies as a function of dark halo mass at various redshifts.

In the present-day universe, since the pioneer work of Fall (1983), the angular momenta of galaxies with various morphological types and masses have been studied by observations and cosmological simulations (e.g. Steinmetz & Navarro 1999; Governato et al. 2007; Romanowsky & Fall 2012; Fall & Romanowsky 2013). Romanowsky

Email: t.okamura@astron.s.u-tokyo.ac.jp

¹Department of Astronomy, Graduate School of Science, The University of Tokyo, 7-3-1 Hongo, Bunkyo-ku, Tokyo 113-0033, Japan

²Research Center for the Early Universe, The University of Tokyo, 7-3-1 Hongo, Bunkyo-ku, Tokyo 113-0033, Japan

& Fall (2012) and Fall & Romanowsky (2013) have extended and updated the study of Fall (1983) with recent observational data. They have found that the specific angular momenta of spiral galaxies are not conserved, with $j_d/m_d \simeq 0.6$ independent of halo mass. This implies that some baryonic processes mentioned above decrease the disk specific angular momentum. Recent semi-analytical and hydrodynamical galaxy formation models have also obtained low angular momentum retention factors (Sales et al. 2012; Colin et al. 2016; Stevens et al. 2016). The roles of baryonic processes that determine the disk specific angular momentum have been examined: they include various types of feedback processes and the formation of bulges by disk instabilities.

On the other hand, beyond $z \sim 1$, there are only a few studies that have observationally examined the specific angular momentum of galaxies because of the difficulty in obtaining kinematic measurements. Burkert et al. (2016) have analyzed the angular momenta of 359 disk star-forming galaxies at $z \sim 0.8 - 2.6$ and found $j_d/m_d \simeq 1$. Contini et al. (2016) have found in 28 low mass galaxies at $z \sim 1$ almost the same stellar mass-angular momentum relation as the local one. However, some semi-analytical and hydrodynamical models predict that disk galaxies at $z \sim 1$ have smaller specific angular momenta than local galaxies (e.g. Sales et al. 2012; Pedrosa & Tissera 2015; Stevens et al. 2016). Some results of cosmological galaxy formation simulations support the picture in which disk galaxies gradually acquire specific angular momentum as they grow. A consensus has not been reached on the angular momentum evolution beyond $z \sim 1$. More observational data are needed to test the model predictions.

In this paper, to tackle the issue of the angular momentum evolution of disk galaxies and understand the formation and evolution of galaxy disks, we study the relation between the fraction of the dark-halo angular momentum transferred to the stellar disk ($j_\star : \star$:star) and the stellar to dark matter halo mass ratio (m_\star) at $z \sim 2, 3$, and 4. We estimate dark halo masses by two independent methods: clustering analysis and abundance matching technique. In order to measure j_\star , it is popular to analyze galaxy kinematics with spectroscopy. However, it is very difficult to construct a large spectroscopic sample at high redshifts. Instead, we make use of the analytical model of Mo et al. (1998) that connects disk size with angular momentum. By measuring the disk sizes of galaxies and assuming this analytic model, we estimate j_\star .

Kravtsov (2013) has investigated stellar disk size to halo size ratios (r_d/r_{dh}), which also reflect angular momentum retention factors, for local galaxies with a similar approach. Kawamata et al. (2015) and Shibuya et al. (2015) have extended his study to high redshift galaxies and found that the disk size to halo size ratios are almost flat out to high redshift. Recently, Huang et al. (2017) and Somerville et al. (2017) have examined the disk size to halo size ratios as a function of stellar mass in more detail out to $z \sim 3$ from CANDELS surveys using abundance matching. They have found that the disk sizes are proportional to the halo sizes from $z \sim 0 - 3$ and the ratios slightly decrease toward $z \sim 0$ and high stellar masses. Our studies are complementary to these studies. There are some new aspects in our work. We

study the mass-angular momentum relation at high redshift. Moreover, while all previous studies have used abundance matching analysis, we use clustering analysis, which is independent of abundance matching analysis to estimate dark halo masses. We also compare our results with recent cosmological galaxy formation simulations.

The structure of our paper is as follows. In Section 2, we construct galaxy samples for this study. After measuring sizes in Section 3, we derive the stellar mass-size relation at each redshift bin in Section 4. The evolution of disk sizes is also discussed. In Section 5, we estimate dark halo masses from clustering analysis and abundance matching results. In Section 6, we present j_\star and m_\star estimates and compare them with recent cosmological galaxy formation simulations. Disk instabilities are also discussed. Conclusions are shown in Section 7.

Throughout this paper, we adopt the cosmology $(\Omega_m, \Omega_\Lambda, h, \sigma_8) = (0.3, 0.7, 0.7, 0.8)$. Magnitudes are in the AB system (Oke & Gunn 1983). Galaxy sizes are given in the physical scale.

2. DATA AND SAMPLES

2.1. Data

We use data from the 3D-HST and CANDELS programs (Grogin et al. 2011; Koekemoer et al. 2011; Brammer et al. 2012; Skelton et al. 2014). Skelton et al. (2014) provide a photometric catalog of the 3D-HST and CANDELS imaging data for five sky fields (COSMOS, GOODS-North, GOODS-South, AEGIS, and UDS) with a total area of ~ 900 arcmin². As these fields have wealthy available data of optical to near-infrared broadband photometry, one can obtain a precise spectral energy distribution (SED) for many high-redshift galaxies. The number of optical to near-infrared broadband filters ranges from 18 in UDS up to 44 in COSMOS. We make use of photometric redshift, stellar mass, and star formation rates (SFR), all of which are available through the 3D-HST Web site.³ Sources have been detected with SExtractor (Bertin & Arnouts 1996) from the combined F125W, F140W, and F160W images. Among the five fields we only use COSMOS, GOODS-South, and AEGIS fields because the clustering properties of galaxies in the remaining two fields appear to largely deviate from the cosmic average as detailed in Appendix.

Photometric redshifts have been determined from the EAZY (Brammer et al. 2008) package, a public photometric redshift code. From the output catalog of EAZY, we adopt `z_peak` as photometric redshifts. Stellar masses and SFRs have been obtained by using the FAST code (Kriek et al. 2009). See Skelton et al. (2014) for details of the procedure. In this paper, we assume a Chabrier (2003) initial mass function (IMF). From here, we take photometric redshifts as redshifts.

2.2. Sample selection

We limit our sample to $H_{160} < 26.0$, which is nearly equal to the 5σ complete magnitude in the shallowest field COSMOS (Skelton et al. 2014). As size measurements need images with high signal to noise ratios (S/N), the 5σ limit is marginally acceptable and slightly shallower compared to other size measurement studies (van

³ <http://3dhst.research.yale.edu>

der Wel et al. 2014; Shibuya et al. 2015). Stellar masses are limited to $M_\star > 10^{8.3} M_\odot$. In the H_{160} – M_\star diagram (Figure 1), stellar masses are largely complete down to $M_\star \simeq 10^{9.0} M_\odot$ for $z \sim 2$ and down to $M_\star \simeq 10^{10} M_\odot$ for $z \sim 3$ and 4. Below those values, our samples are biased toward low M/L galaxies. We exclude galaxies with $M_\star > 10^{10.4} M_\odot$ from our samples for $z \sim 3$ and 4 because the number of galaxies is insufficient for clustering analysis.

We use the stellar mass–SFR diagram to remove quiescent galaxies. On the basis of the stellar masses and the SFRs obtained from the FAST, we construct stellar mass–SFR diagrams for our samples, as shown in Figure 2. First, we fit the stellar mass–SFR distribution by a power law, which defines the main-sequence. At $z \sim 2$ and 3, galaxies that lie above the -2σ of the main-sequence are considered to be star-forming galaxies, where the standard deviation of the MS is $\sigma \simeq 0.33$ dex for both redshifts. For $z \sim 4$, we remove galaxies that have small SFRs by eye. In this paper, we do not consider the effects of bulges because main sequence galaxies above $z \sim 2$ have low B/T ratios (Brennan et al. 2017).

We exclude regions that have a shallow or deep exposure time for each field because clustering analysis requires images with a uniform depth. We also construct masks to avoid the vicinity of bright stars and diffraction spicks. For each redshift, we divide the entire sample into four ($z \sim 2$) or three ($z \sim 3$ and 4) subsamples according to stellar mass. The number of galaxies in the final samples is summarized in Table 1.

3. SIZE MEASUREMENTS

3.1. Size measurements with GALFIT

Galaxy sizes are measured for the F160W imaging data provided by the 3D-HST. Position, flux, half-light radius (r_d), Sérsic index (n), axis ratio ($q \equiv b/a$), and position angle are treated as free parameters to determine. In this paper, we use the half-light radius along the semi-major axis of the Sérsic profile to define the size of galaxies. We make 100 pixels \times 100 pixels cutout images around object galaxies before size measurement. We then run GALFIT (Peng et al. 2002, 2010) on those cutout images, where neighbors are masked as not to perturb the fitting of the target galaxies. The masks are created from SExtractor segmentation maps.

As an initial guess of the free parameters, we use SExtractor output parameters given in the 3D-HST catalog. Results of GALFIT are not sensitive to initial values as long as they are not far from real values (Häussler et al., 2007). We vary individual parameters over the following ranges: $\Delta x, \Delta y < 3$ pixels, $0.3 < r_d < 100$ pixel, $0.1 < n < 8$, $0.1 < q < 1$, where Δx and Δy are the difference in the centroids between SExtractor and GALFIT. We define galaxies whose best-fit parameters are within these ranges as “success”. We only use “success” galaxies in the following analysis in Sections 3 and 4. The number of “success” galaxies is summarized in Table 1. While we obtain robust structural parameters of only a part of our clustering sample, the average SExtractor sizes of the “success” sample and the entire sample are nearly equal. Thus we use the GALFIT sizes of the “success” sample as the representatives of the entire

sample.

3.2. Deriving r_d at rest-frame 5000Å

We derive r_d at the rest-frame 5000Å at all redshifts. While we measure sizes in observed $1.6\mu m$ (F160W band), there exists a color gradient that depends on stellar mass and redshift. We obtain rest 5000Å r_d by using the formula given in van der Wel et al. (2014):

$$r_d = r_{d,F160W} \left(\frac{1+z}{1+z_p} \right)^{\Delta \log r_d / \Delta \log \lambda} \quad (3)$$

where z_p is the “pivot redshift” (2.2 for F160W) and the wavelength dependence is given by:

$$\frac{\Delta \log r_d}{\Delta \log \lambda} = -0.35 + 0.12z - 0.25 \log \left(\frac{M_\star}{10^{10} M_\odot} \right). \quad (4)$$

Although van der Wel et al. (2014) have only examined wavelength dependence over $0 < z < 2$, we extend this formula to $z \simeq 4$ because the redshift evolution of this relation looks linear as a function of redshift. In any case, the correction values at $z \sim 3$ and 4 are relatively small.

4. STELLAR MASS–SIZE RELATION

The stellar mass–size distributions of our star-forming galaxies are shown in Figure 3. In Section 4.1, we analyze these distributions by modeling them with a power law. Then, we discuss the results in Section 4.2.

4.1. Analytical Model of the stellar mass–size relation

The stellar mass–size relation is usually modeled as a single power-law:

$$\bar{r}_d(M_{\star,10})/\text{kpc} = A \cdot M_{\star,10}^\alpha, \quad (5)$$

where $M_{\star,10} = M_\star / 1.0 \times 10^{10} M_\odot$, and $\bar{r}_d(M_{\star,10})$ is the median size at $M_{\star,10}$. For the size distribution at a given stellar mass, we adopt a log-normal distribution:

$$p(r_d | \sigma_{\ln r}, \bar{r}_d) dr_d = \frac{1}{\sqrt{2\pi} \sigma_{\ln r} r_d} \exp \left[-\frac{(\ln r_d - \ln \bar{r}_d)^2}{2\sigma_{\ln r}^2} \right] dr_d, \quad (6)$$

where $p(r_d | \sigma_{\ln r}, \bar{r}_d) dr_d$ is the probability density that a galaxy has a size between $(r_d, r_d + dr_d)$ at the given stellar mass, and $\sigma_{\ln r}$ is the dispersion of the distribution. The reason for adopting a log-normal distribution comes from Equation (2). The disk size is proportional to the dimensionless spin parameter λ , and the distribution of λ is well approximated by a log-normal distribution according to N -body simulations (Barnes & Efstathiou 1987; Bullock et al. 2001).

We assume that each of the observed disk sizes has a gaussian error:

$$g(x | \delta r_d) dx = \frac{1}{\sqrt{2\pi} \delta r_d} \exp \left(-\frac{x^2}{2\delta r_d^2} \right) dx, \quad (7)$$

where $g(x | \delta r_d) dx$ is the probability density that a galaxy has an intrinsic disk size between x and $x + dx$. The probability of observing $(r_d, \delta r_d)$ assuming the log-normal distribution $p(r_d | \sigma_{\ln r}, \bar{r}_d)$ is given by the convolution of the two functions:

$$(p * g)(r_d) = \int p(x) g(r_d - x) dx. \quad (8)$$

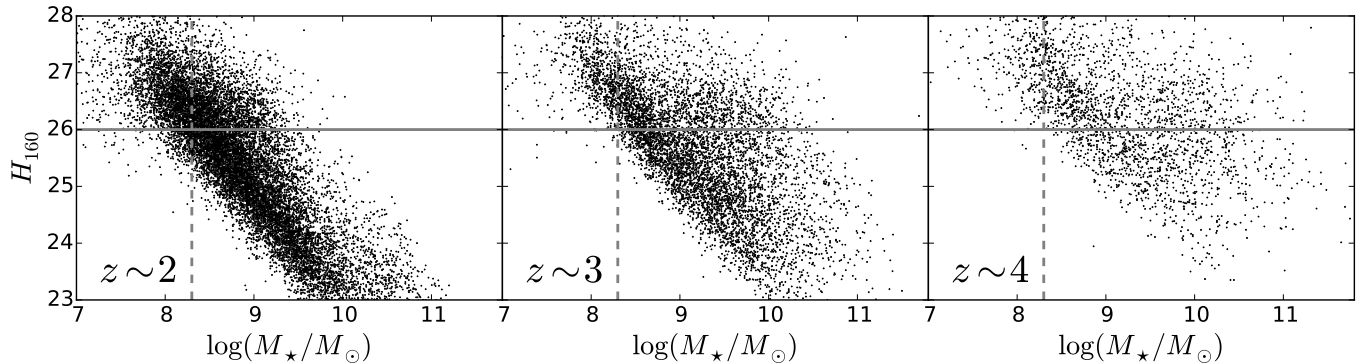


Figure 1. $H_{160} - M_*$ diagram at $z \sim 2, 3,$ and 4 (left to right). The vertical dashed lines and horizontal solid lines indicate the stellar mass limits and the observed H_{F160W} magnitude limits, respectively.

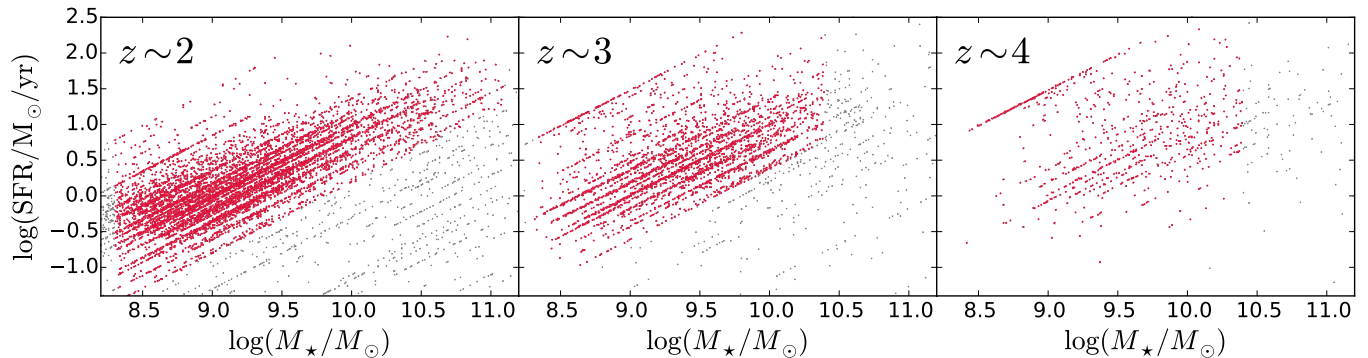


Figure 2. Star-formation rate vs. stellar mass diagram at $z \sim 2, 3,$ and 4 (left to right). Objects used in our study are shown in red.

Table 1
Number of star-forming galaxies for stellar mass subsamples

z	$\log(M_*/M_\odot)$	Number (Clustering) ^a	Number (Size “success”) ^b
2.0	10.4 – 11.1	264	198
	9.7 – 10.4	1086	870
	9.0 – 9.7	3267	2458
3.0	8.3 – 9.0	3173	1772
	9.7 – 10.4	805	560
	9.0 – 9.7	1596	1060
4.0	8.3 – 9.0	838	412
	9.7 – 10.4	273	161
	9.0 – 9.7	348	176
	8.3 – 9.0	133	70

^a Number of star-forming galaxies used for clustering analysis.

^b Number of star-forming galaxies that have robust fitting parameters with GALFIT detailed in Section 3.1

We use the 1σ error in GALFIT as δr_d . For each redshift, the free parameters of this model are given by $\mathbf{P} = (A, \alpha, \sigma_{\ln r, i})$, where, i denotes i -th subsample; we assume that different stellar mass bins have different $\sigma_{\ln r}$ values. We have six free parameters at $z \sim 2$, and five free parameters at $z \sim 3$ and 4 . We use the maximum likelihood estimation (MLE) to determine these parameters, where the estimated parameters make the observed r_d distribution the most probable. For subsample i at a given redshift, the likelihood function is defined as

$$\mathcal{L}_i = \prod_{j=1}^N (p * g)(r_{d,j} | \sigma_{\ln r, i}, \bar{r}_d), \quad (9)$$

where j represents the j -th object. We determine the parameter set \mathbf{P} that maximizes the likelihood function $\mathcal{L} \equiv \prod \mathcal{L}_i$. The best-fit values are listed in Table 2. We use the `scipy.optimize` package and the L-BFGS-B algorithm (Zhu et al. 1997) to find the maximizing point. The uncertainties in the parameters are estimated by the Markov Chain Monte Carlo (MCMC) sampling. MCMC is a powerful algorithm to approximate multi-dimensional parameters using a Markov chain. We use the python package `emcee` (Foreman-Mackey et al. 2013) to run MCMC. In Figure 4, we show for each parameter the best-fit values and the 68%, 95%, and 99% confidence intervals. This figure is made using the public python package `corner` (Foreman-Mackey 2016).

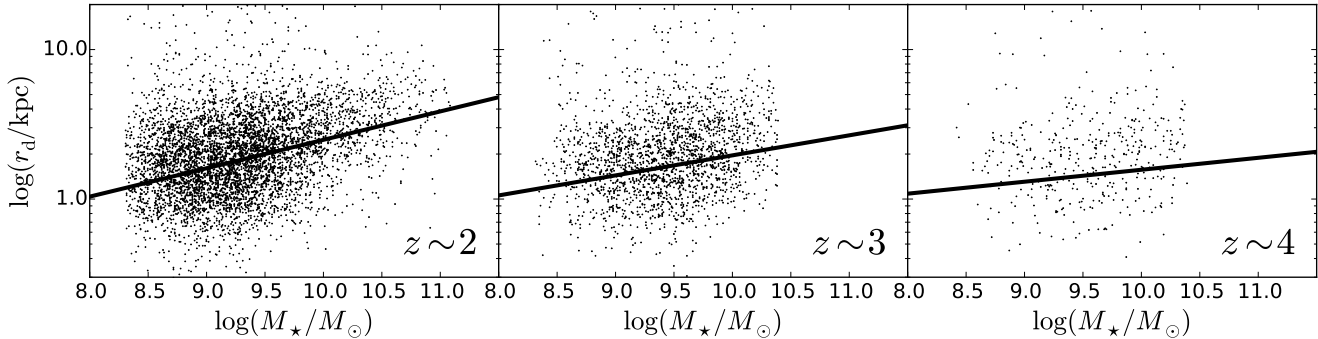


Figure 3. Stellar mass–size distribution of disk galaxies at $z \sim 2, 3,$ and 4 (left to right). The solid lines indicate the best-fit power-laws.

Table 2
Best-fit parameters of the stellar mass–size relation

z	A	α	$\sigma_{8.3 < M_* < 9.0}$	$\sigma_{9.0 < M_* < 9.7}$	$\sigma_{9.7 < M_* < 10.4}$	$\sigma_{10.4 < M_* < 11.1}$
2.0	$2.51^{+0.03}_{-0.05}$	$0.19^{+0.01}_{-0.01}$	$0.46^{+0.01}_{-0.01}$	$0.51^{+0.01}_{-0.01}$	$0.50^{+0.02}_{-0.02}$	$0.53^{+0.03}_{-0.05}$
3.0	$1.94^{+0.06}_{-0.05}$	$0.14^{+0.01}_{-0.03}$	$0.42^{+0.03}_{-0.03}$	$0.47^{+0.02}_{-0.02}$	$0.47^{+0.02}_{-0.02}$...
4.0	$1.57^{+0.11}_{-0.13}$	$0.08^{+0.05}_{-0.05}$	$0.45^{+0.18}_{-0.05}$	$0.51^{+0.08}_{-0.07}$	$0.47^{+0.09}_{-0.06}$...

4.2. Size evolution

The evolution of A , α , and $\sigma_{\ln r}$ are shown in Figure 5. In this Section, we discuss the evolution of each parameter in detail.

4.2.1. Median size evolution

The size evolution at a fixed stellar mass is generally parameterized as $(1+z)^{-\beta_z}$, where β_z is a constant expressing the strength of evolution (evolution slope). The top panel of Figure 5 represents the median size evolution of disk star-forming galaxies at $M_* = 1.0 \times 10^{10} M_\odot$. The solid blue line shows the best-fit function over $z \sim 2-4$: $\bar{r}_d(M_{*,10})/\text{kpc} = 6.88(1+z)^{-0.91 \pm 0.01}$. Allen et al. (2016) have measured the size evolution of a mass-complete sample ($\log(M_*/M_\odot) > 10$) of star-forming galaxies over redshifts $z = 1-7$, to find that the average size at a fixed mass of $\log(M_*/M_\odot) = 10.1$ is expressed by $r_d = 7.07(1+z)^{-0.89 \pm 0.01}$. The slope we find is in agreement with Allen et al. (2016)’s value. Shibuya et al. (2015) have also measured the stellar mass–median circularized size evolution of star-forming galaxies with $9.0 < \log(M_*/M_\odot) < 11.0$ at $0 < z < 6$. The gray dotted line represents the average circularized half-light radius from their samples with the gray region showing the 16th and 84th percentiles. The evolution slope is consistent with our result. The difference in the amplitude is largely due to the different definition of galaxy sizes. We also note that Shibuya et al. (2015) have used the Salpeter IMF (Salpeter 1955) to derive stellar masses.

However, $\beta_z = 0.91 \pm 0.01$ is slightly steeper than the value by van der Wel et al. (2014). They have studied a mass complete sample of star-forming galaxies and have found $(1+z)^{-0.75}$ at a $\log(M_*/M_\odot) = 10.7$ over the redshift range $0 < z < 3$. As their method of size measurements is the same as ours, we attribute this discrepancy to the difference in the redshift range. The evolution slope of star-forming galaxies appears to become steeper

above $z \sim 2$ or 3 . Allen et al. (2016)’s sample also shows steeper slopes at higher redshifts (See Figure 3 of Allen et al. 2016).

As size evolution is closely related to the evolution of hosting dark matter halos, β_z contains information of dark matter halos. From Equation (2), when r_d/r_{200} is constant irrespective of z and M_{dh} , r_d is given by

$$r_d \propto H(z)^{-1} V_c \quad (10)$$

$$\propto H(z)^{-2/3} M_{\text{dh}}^{1/3}, \quad (11)$$

where V_c is the circular velocity of dark matter halos. The Hubble parameter as a function of z , $H(z) = H_0 \sqrt{\Omega_m(1+z)^3 + \Omega_\Lambda}$, is approximated as $H(z) \propto (1+z)^{1.5}$. According to Equations (10) and (11), $r_d \propto (1+z)^{-1.5}$ means evolution at a constant circular velocity and $r_d \propto (1+z)^{-1.0}$ means evolution at a constant virial mass (Ferguson et al. 2004). The $\beta_z = 0.91$ is close to the prediction for a constant virial mass.

4.2.2. Slope evolution

The middle panel of Figure 5 shows the slope evolution in the stellar mass–size relation (α). The slope evolution of the stellar mass–size relation for late-type galaxies was first investigated by van der Wel et al. (2014). They have found that the slope has nearly a constant value $\simeq 0.2$ over the redshift range $0 < z < 3$. Similarly Allen et al. (2016) have found $\alpha = 0.15 \pm 0.01$ for star-forming galaxies at $1 < z < 2.5$. Our results are consistent with those of van der Wel et al. (2014) and Allen et al. (2016) at $z \sim 2$ and 3 , however, being slightly lower at $z \sim 4$.

The slope evolution of the stellar mass–size relation is determined as a combination of the slope of the stellar mass–halo mass relation and the slope of the disk size–halo size relation. In this paper, We have measured all three slopes. We will discuss the relation between the three slopes in Section 6.

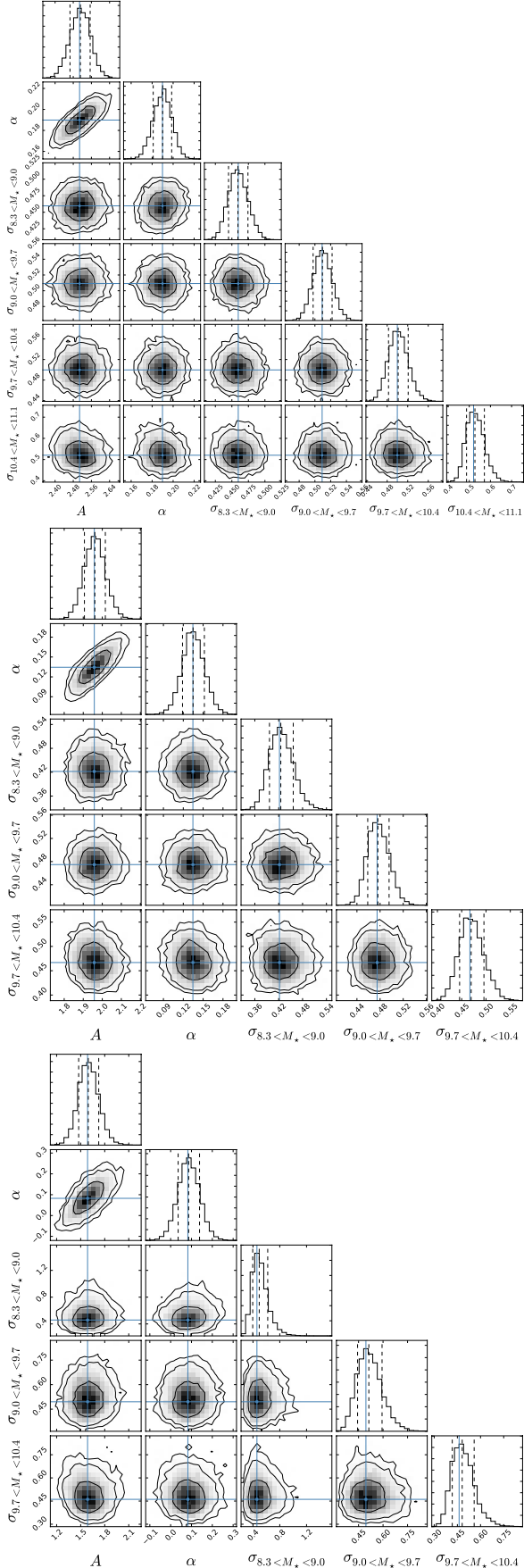


Figure 4. Sixty-eight percent, 96%, and 99% confidence intervals for individual parameters at $z \sim 2, 3,$ and 4 (top to bottom). The top panel of each column shows the probability distribution function of each parameter. The solid blue lines indicate the median values.

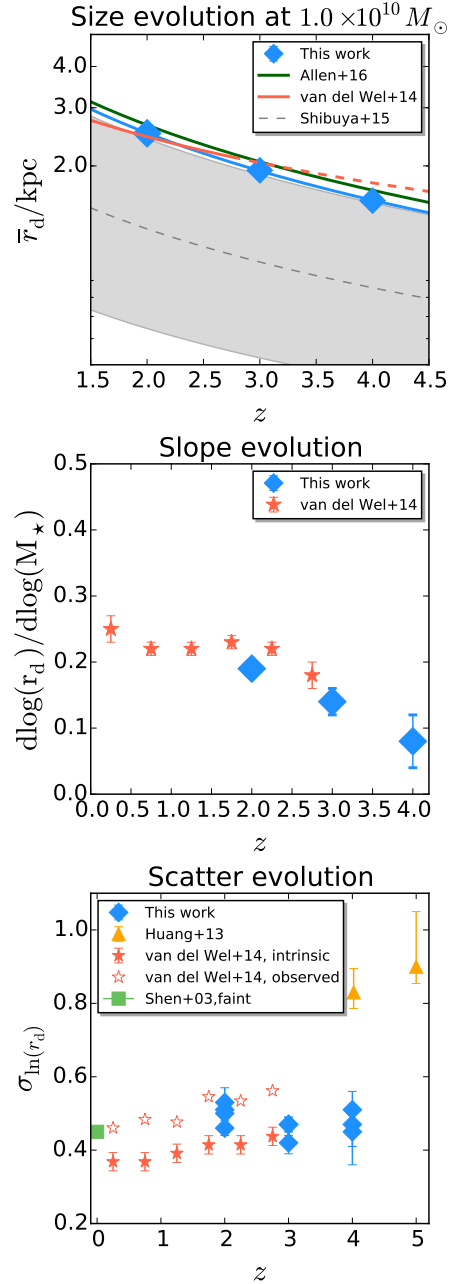


Figure 5. Redshift evolution of the stellar mass–size relation of star-forming galaxies. Top: the size evolution at $M_* = 1.0 \times 10^{10} M_\odot$. The blue diamond symbols indicate the results obtained in this paper, and the solid blue line shows the best-fit power law. The green solid line shows the average size of star forming galaxies from Allen et al. (2016) at $10^{10.1} M_\odot$. The red solid line indicates the size evolution of late-type galaxies from van der Wel et al. (2014) at $10^{9.75} M_\odot$, and the red dashed line is its extrapolation. The gray dotted line and the shaded region indicate the median circularized size and the 16th and 84th percentiles distribution of star-forming galaxies with $9.5 < \log M_*/M_\odot < 10.0$ (Shibuya et al. 2015). Middle: slope evolution. The blue and red symbols represent our galaxies and late-type galaxies from van der Wel et al. (2014), respectively. Bottom: the intrinsic scatter evolution from this work and previous studies. The blue symbols represent our galaxies. The orange symbols represent LBGs from Huang et al. (2013) at $z \sim 4$ and 5 . The filled and open red symbols show the late-type galaxies of van der Wel et al. (2014). The green symbol shows the SDSS galaxies of Shen et al. (2003) at the faint end.

4.2.3. Scatter evolution

We present the evolution of the intrinsic scatter in the bottom panel of Figure 5: here, “intrinsic” means that measurement errors have been removed. The scatter for local galaxies is generally small. Shen et al. (2003) have found $\sigma_{\ln r_d} \sim 0.3$ for both late-type and early type galaxies from SDSS. This result has also been ascertained by the result of Courteau et al. (2007), $\sigma_{\ln r_d} \sim 0.3$, for local spiral galaxies. These studies have been extended by van der Wel et al. (2014) to the high-redshift universe and they have found that the intrinsic scatter does not strongly evolve since $z \sim 2.75$ for both late-type and early-type galaxies. In their study, the scatter for late type galaxies is 0.16 – 0.19 dex, which is comparable to the result of Shen et al. (2003) and Courteau et al. (2007). We extend van der Wel et al. (2014)’s study up to $z \sim 4$, and find that the intrinsic scatter is constant with 0.4 – 0.6 over $z \sim 2 - 4$.

The scatter of λ has been specifically investigated by N -body simulations and found to be $\sigma_\lambda \sim 0.5$ (Bullock et al. 2001). Thus the disk formation model of Equation (2) naively predicts that the intrinsic scatter of sizes is ~ 0.5 .

The results for local galaxies imply that the size scatter is smaller than that of the spin parameter λ . To explain the observed small scatters, some mechanisms are needed. One possible mechanism is bulge growth. The growth of bulges increases the specific angular momentum of disks and thus expands disk sizes. Low-spin galaxies selectively grow their bulges. Some kind of disk instability and feedback has also been proposed which remove galaxies with low-spin and high-spin halos.

Our result, $\sigma_{\ln r_d} \sim 0.4 - 0.6$, is comparable with the scatter of the log-normal distribution of λ . This implies that for star-forming galaxies at $z \sim 2 - 4$ the size scatter at a given stellar mass is fully explained by the scatter of λ . Our result, however, does not agree with the large scatters, $\sigma_{\ln r_d} \sim 0.8 - 0.9$, found by Huang et al. (2013) for the size–UV luminosity relations of $z \sim 4 - 5$ LBGs. This may suggest that the UV luminosity–halo mass relation of LBGs has a considerably large scatter.

5. HALO MASS ESTIMATES

In this Section we estimate the masses of the dark matter halos hosting our galaxies by using two independent methods: clustering analysis and abundance matching technique. Clustering analysis utilizes the large scale clustering amplitude of observed galaxies to obtain their hosting dark matter halo masses. Clustering analysis is a popular way to estimate hosting dark matter halo masses, however the mass estimates in this paper have relatively large errors because the sizes of individual subsamples are not so large. To test the results of the clustering analysis, we use abundance matching technique, which connects the stellar mass of galaxies to that of dark matter halos. While abundance matching can easily estimate hosting dark matter halo masses, it does not consider that different galaxy types have different stellar mass dark halo mass ratios. We briefly explain the two methods and show the obtained dark matter halo masses.

5.1. Clustering analysis

5.1.1. Angular correlation function

We compute the two point angular correlation functions (ACFs), $\omega_{\text{true}}(\theta)$, of star-forming galaxies. Here, we assume all of our galaxies as central galaxies. The observed ACFs, $\omega_{\text{obs}}(\theta)$, are measured by counting the number of unique pairs of observed galaxies and comparing it with what is expected from random samples. We adopt the estimator proposed by Landy & Szalay (1993):

$$\omega_{\text{obs}}(\theta) = \frac{DD(\theta) - 2DR(\theta) + RR(\theta)}{RR(\theta)}, \quad (12)$$

where $DD(\theta)$, $DR(\theta)$, and $RR(\theta)$ are the normalized numbers of galaxy-galaxy, galaxy-random and random-random pairs, respectively, with separation θ . We generate 1000 times as many random points as the number of galaxies accounting for the geometry of the observed area and the masks. The formal error in ω_{true} is given by

$$\sigma_\omega = \sqrt{[1 + \omega_{\text{obs}}]/DD(\theta)}. \quad (13)$$

We assume a power law parameterization for the ACF,

$$\omega_{\text{true}}(\theta) = A_\omega \theta^{-\beta}. \quad (14)$$

We fix $\beta = 0.8$ following previous studies (e.g. Peebles 1975; Ouchi et al. 2001, 2004, 2010; Foucaud et al. 2003, 2010; Harikane et al. 2016).

It is known that ω_{obs} is underestimated because we only use a finite survey area. This is compensated by introducing an integral constraint (IC) (Groth & Peebles 1977):

$$\omega_{\text{true}} = \omega_{\text{obs}} + \text{IC}. \quad (15)$$

The IC value depends on the size and shape of the survey area, and is estimated using a random catalog:

$$\text{IC} = \frac{\sum_i RR(\theta_i) \omega_{\text{true}}(\theta_i)}{\sum_i RR(\theta_i)} = \frac{\sum_i RR(\theta_i) A_\omega \theta^{-\beta}}{\sum_i RR(\theta_i)}. \quad (16)$$

Because the three 3D-HST fields used in this paper have almost the same size, we obtain nearly the same IC value ($\text{IC}_{\text{GOODS-S}} = 0.016A_\omega$, $\text{IC}_{\text{COSMOS}} = 0.013A_\omega$, and $\text{IC}_{\text{AEGIS}} = 0.010A_\omega$). The amplitude A_ω is estimated through the ACFs of the three fields by minimizing χ^2 :

$$\chi^2 = \sum_{i,j=\text{fields}} \frac{[A_\omega \theta_i^{-\beta} - (\omega_{\text{obs},j}(\theta_i) + \text{IC}_j)]^2}{\sigma_{\omega,j}^2(\theta_i)}, \quad (17)$$

where IC_j , $\omega_{\text{obs},j}$, and $\sigma_{\omega,j}^2(\theta)$ denote the IC, observed ACF, and errors in field j , respectively. We use data at $\theta > 10''$ for fitting because at $\theta < 10''$ the contribution of the one halo term cannot be ignored. In figure 6 we plot the ACFs of our subsamples with the best-fit power laws.

Then we estimate the spatial correlation function, $\xi(r)$, from the measured ACFs and the redshift distribution of galaxies. The spatial correlation function is usually assumed to be a single power law as

$$\xi(r) = \left(\frac{r}{r_0}\right)^{-\gamma}, \quad (18)$$

where r_0 is the correlation length and γ is the slope of the power law. These parameters are related to those of

the two point angular correlation function via the Limber transform (Peebles 1980; Efstathiou et al. 1991).

$$\beta = \gamma - 1, \quad (19)$$

$$A_w = \frac{r_0^\gamma B[1/2, (\gamma - 1)] \int_0^\infty dz N(z)^2 F(z) D_\theta(z)^{1-\gamma} g(z)}{[\int_0^\infty N(z) dz]^2}, \quad (20)$$

$$g(z) = \frac{H_0}{c} (1+z)^2 \{1 + \Omega_m z + \Omega_\Lambda [(1+z)^{-2} - 1]\}^{1/2} \quad (21)$$

where $D_\theta(z)$ is the angular diameter distance, $N(z)$ is the redshift distribution of galaxies, B is the beta function, and $F(z)$ describes the redshift evolution of $\xi(r)$. $F(z)$ is often modeled as $F(z) = [(1+z)/(1+z_c)]^{-(3+\bar{\epsilon})}$ with $\bar{\epsilon} = -1.2$ (Roche & Eales 1999), where z_c is the characteristic redshift of galaxies. We assume that the clustering evolution is fixed in comoving coordinates over the redshift range in question.

5.1.2. Galaxy biases and halo masses

To understand the relation between galaxies and hosting dark matter halos we use the halo model of Sheth et al. (2001), which is obtained from the ellipsoidal collapse model. In the model of Sheth et al. (2001) the bias factor of dark halos, b_{dh} , is given by

$$b_{\text{dh}} = 1 + \frac{1}{\delta_c} \left[\nu'^2 + b\nu'^{2(1-c)} - \frac{\nu'^{2c}/\sqrt{a}}{\nu'^{2c} + b(1-c)(1-c/2)} \right], \quad (22)$$

where $\nu' = \sqrt{a}\nu$, $a = 0.707$, $b = 0.5$, $c = 0.6$, and $\delta_c = 1.69$ is the critical amplitude above which overdense regions collapse to form a virialized object. Here, ν is defined as

$$\nu = \frac{\delta_c}{\sigma(M, z)} = \frac{\delta_c}{D(z)\sigma(M, 0)}, \quad (23)$$

where $D(z)$ is the linear growth factor, $\sigma(z)$ is the mass rms. of the smoothed density field. We calculate $D(z)$ by the formula of Carroll et al. (1992) and $\sigma(M, 0)$ using an initial power spectrum of a power law index $n = 1$ and the transfer function of Bardeen et al. (1986). Then we define the linear galaxy bias, which is the relation between the clustering amplitude of galaxies and that of dark matter halos, at a large scale ($= 8h_{100}^{-1}$ Mpc) as

$$b_g = \sqrt{\frac{\xi_g(r = 8h_{100}^{-1} \text{ Mpc})}{\xi_{\text{DM}}(r = 8h_{100}^{-1} \text{ Mpc})}} = \sqrt{\frac{[8h_{100}^{-1} \text{ Mpc}/r_0]^{-\gamma}}{\xi_{\text{DM}}(r = 8h_{100}^{-1} \text{ Mpc})}}, \quad (24)$$

where $\xi_{\text{DM}}(r = 8h_{100}^{-1} \text{ Mpc})$ is the dark matter spatial correlation function. We calculate $\xi_{\text{DM}}(r = 8h_{100}^{-1} \text{ Mpc})$ using the non-linear model of Smith et al. (2003). Assuming that the galaxy bias at large scales is almost the same as the halo bias ($b_g \simeq b_{\text{dh}}$), we obtain an estimate of dark halo masses. The correlation length and the estimated halo masses are summarized in Table 3.

5.2. Abundance Matching

In order to reinforce the results of the clustering analysis, we also use abundance matching analysis, which

connects the number density of galaxies to that of dark halos to estimate the hosting dark halo mass for a given stellar mass. We adopt the abundance matching result of Behroozi et al. (2013). Many researchers that study the angular momentum retention factor adopt the abundance matching analysis of Dutton et al. (2010) and Behroozi et al. (2013) to estimate halo masses (e.g. Romanowsky & Fall 2012; Burkert et al. 2016). This makes easy to compare our results with previous results of angular momentum studies. The estimated halo masses are also summarized in Table 3.

Figure 7 shows a comparison of the estimated dark matter halo masses. The estimated dark matter halo masses by the two independent methods are consistent within the error bars except for the highest stellar mass bins at $z \sim 2$. This makes the results of the clustering analysis more plausible. In the following Section, we display the results based on the both methods.

6. ANGULAR MOMENTUM

6.1. Estimation of the specific angular momentum

In this Section, we briefly explain the way to estimate the disk specific angular momentum. As already mentioned in Section 1, the disk size of a galaxy reflects its specific angular momentum. According to the model of Mo et al. (1998), the specific angular momentum of disk galaxies with an exponential profile ($n = 1$) is given by:

$$j_d = \frac{\sqrt{2}}{1.678} r_d m_d \lambda^{-1} r_{200}^{-1} f_c(c_{\text{vir}})^{1/2} f_R(\lambda, c_{\text{vir}}, m_d, j_d)^{-1}. \quad (25)$$

If we assume r_d as the half-light radius of a Sérsic index n , we can expand this equation to:

$$j_d = f_n(n)^{-1} r_d m_d \lambda^{-1} r_{200}^{-1} f_c(c_{\text{vir}})^{1/2} f_R(\lambda, c_{\text{vir}}, m_d, j_d)^{-1}, \quad (26)$$

$$f_n(n) = \frac{\sqrt{2}\Gamma(2n)\kappa^n}{\Gamma(3n)}, \quad (27)$$

where Γ is a gamma function, and κ is well approximated by

$$\kappa = 2n - \frac{1}{3} + \frac{4}{405n} + \frac{46}{25525n^2} + \frac{131}{1148175n^3} + \mathcal{O}(n^{-4}) \quad (n > 0.36), \quad (28)$$

$$\kappa = 0.01945 - 0.8902n + 10.95n^2 - 19.67n^3 + 13.43n^4 \quad (n < 0.36) \quad (29)$$

(Ciotti & Bertin 1999; MacArthur et al. 2003). The full functional forms of f_c and f_R are given in Mo et al. (1998). The values of λ and c_{vir} are well determined by N -body simulations (Vitvitska et al. 2002; Davis & Natarajan 2009; Prada et al. 2012; Rodríguez-Puebla et al. 2016). We adopt $(\lambda, c_{\text{vir}}) = (0.035, 4.0)$ throughout the examined redshift range ($z \sim 2 - 4$). From the dark matter halo masses estimated in Section 5, we can calculate m_d and r_{200} , where r_{200} is calculated by

$$r_{200} = \left(\frac{GM_{\text{dh}}}{100H(z)^2} \right)^{1/3}. \quad (30)$$

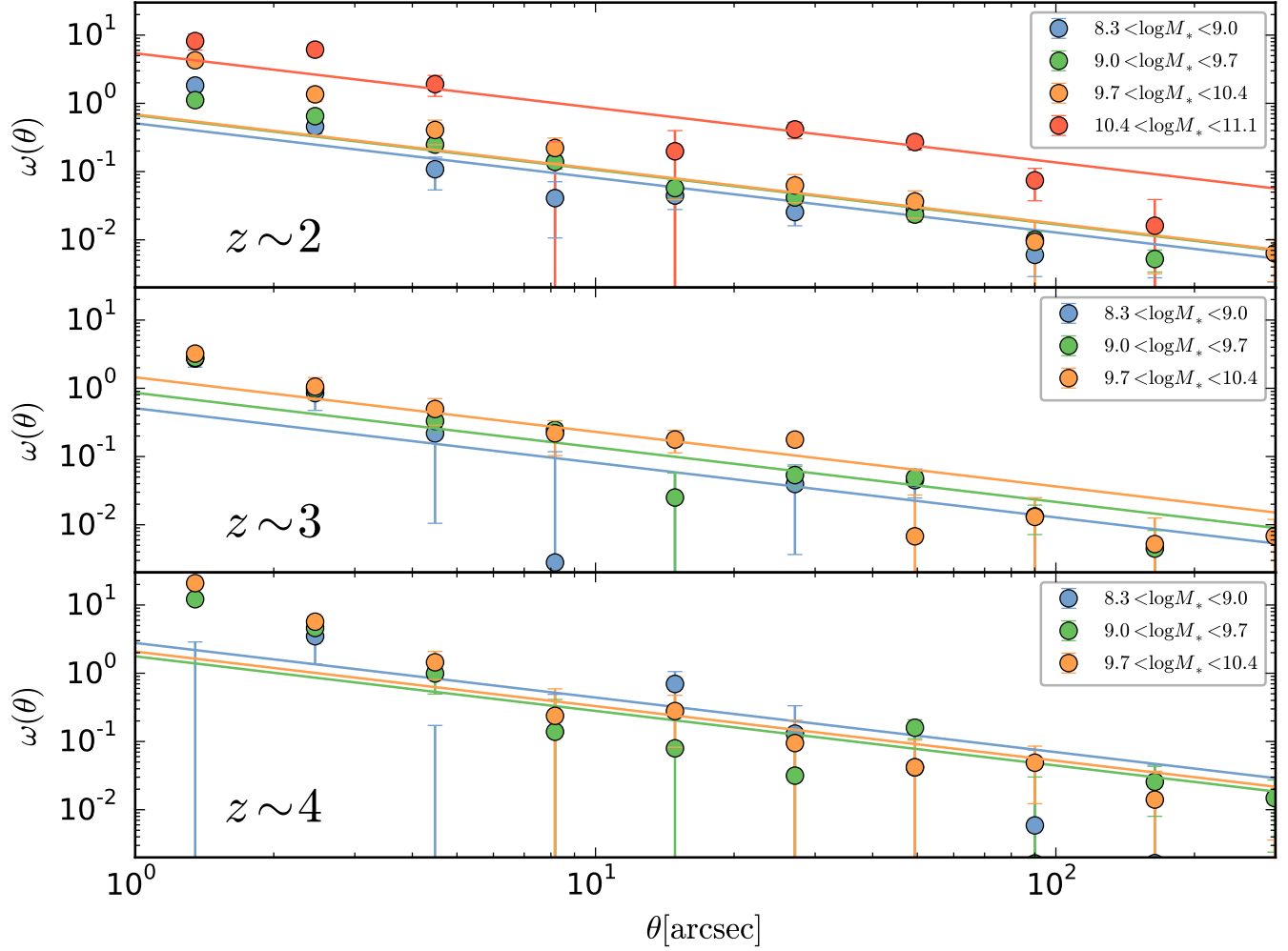


Figure 6. Angular correlation functions of star-forming galaxies at $z \sim 2, 3,$ and 4 (top to bottom). Data points and the best-fit power laws are color-coded by the stellar mass range.

Table 3
Summary of the clustering analysis and the abundance matching analysis

z	$\log(M_*/M_\odot)$	N	$A_\omega[\text{arcsec}^{0.8}]$	$r_0[h^{-1}\text{Mpc}]$	$\log(M_{\text{dh,CL}}[h^{-1}M_\odot])$	$\log(M_{\text{dh,AM}}[h^{-1}M_\odot])$
2.0	10.58	264	$5.40^{+0.96}_{-0.96}$	$12.30^{+1.18}_{-1.25}$	$13.37^{+0.10}_{-0.12}$	12.23
	9.94	1086	$0.69^{+0.25}_{-0.25}$	$3.92^{+0.73}_{-0.87}$	$11.69^{+0.32}_{-0.56}$	11.79
	9.30	3267	$0.67^{+0.07}_{-0.07}$	$3.86^{+0.21}_{-0.23}$	$11.66^{+0.11}_{-0.13}$	11.51
	8.72	3173	$0.51^{+0.08}_{-0.08}$	$3.31^{+0.28}_{-0.30}$	$11.32^{+0.18}_{-0.23}$	11.30
3.0	9.93	805	$1.45^{+0.31}_{-0.31}$	$5.18^{+0.58}_{-0.65}$	$11.92^{+0.17}_{-0.23}$	11.81
	9.37	1596	$0.86^{+0.15}_{-0.15}$	$3.87^{+0.36}_{-0.39}$	$11.40^{+0.17}_{-0.21}$	11.53
	8.78	838	$0.51^{+0.31}_{-0.31}$	$2.90^{+0.87}_{-1.18}$	$10.79^{+0.56}_{-1.60}$	11.29
4.0	10.01	273	$2.08^{+0.93}_{-0.93}$	$5.57^{+1.27}_{-1.56}$	$11.79^{+0.31}_{-0.56}$	11.78
	9.37	348	$1.77^{+0.72}_{-0.72}$	$5.09^{+1.06}_{-1.28}$	$11.64^{+0.30}_{-0.51}$	11.45
	8.82	133	$2.78^{+1.74}_{-1.74}$	$6.54^{+2.03}_{-2.75}$	$12.03^{+0.38}_{-0.91}$	11.22

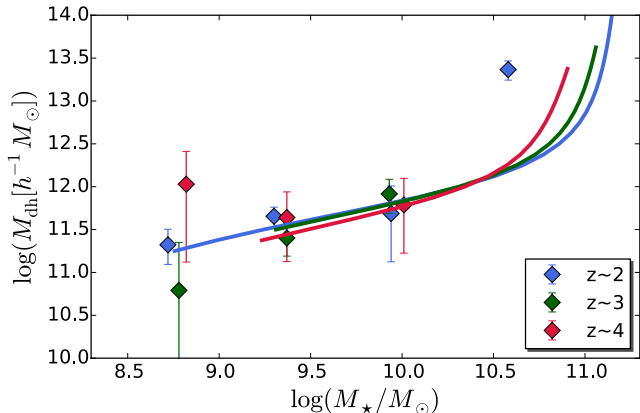


Figure 7. Dark matter halo mass as a function of stellar mass obtained from clustering analysis and abundance matching technique at $z \sim 2, 3,$ and 4 . The diamonds indicate the results of clustering analysis, while the solid lines indicate the results of the abundance matching of Behroozi et al. (2013).

Combined with n and r_d measured in Sections 3 and 4, we can estimate j_d .

6.2. Mass–angular momentum relation

6.2.1. Average j_d/m_d ratio and its evolution

Figure 8 shows the angular momentum retention factor of star-forming galaxies as a function of hosting halo mass. We find $j_*/m_* = 0.77 \pm 0.06$ from clustering analysis and $j_*/m_* = 0.83 \pm 0.13$ from abundance matching at $z \sim 2, 3,$ and 4 . No strong redshift evolution is confirmed. As we mention in Section 1, $j_*/m_* = 1$ means that the angular momentum is fully conserved and $j_*/m_* < 1$ means that galaxies lose their specific angular momentum during their formation and evolution.

Romanowsky & Fall (2012) have investigated kinematical structure for about 100 bright early and late-type galaxies at $z \sim 0$. They have found that late-type galaxies typically have $j_d/m_d \simeq 0.6$ and early-type galaxies have $j_d/m_d \simeq 0.1$. A small j_d/m_d value has also been reported by Dutton & van den Bosch (2012). They have calculated angular momentum retention factor as a function of halo mass by constructing the mass models (Dutton et al. 2011) tuned to observed scaling relations for SDSS galaxies. They have obtained a constant value $j_d/m_d = 0.61^{+0.13}_{-0.11}$ with halo masses $10^{11.3} M_\odot \lesssim M_{\text{dh}} \lesssim 10^{12.7} M_\odot$. Our values at $z \sim 2, 3,$ and 4 are in rough agreement with these local values for late-type galaxies within errors.

There exist a few studies that have investigated the mass–angular momentum relation at high redshifts. Recently, Burkert et al. (2016) have investigated the relation for ~ 360 star-forming galaxies at $z \sim 0.8 - 2.6$, among which about 100 are at $z \sim 2$, by H α kinematics based on KMOS and SINS/zC-SINF surveys. They have found $j_d/m_d = 1.0$ with a statistical uncertainty of ± 0.1 and a systematic uncertainty of ± 0.5 . This j_d/m_d value is consistent with our result at $z \sim 2$.

We then compare our results with those of Huang et al. (2017) and Somerville et al. (2017). These authors have derived disk size to halo size ratios (r_d/r_{dh}) as a function of stellar mass over $z \sim 0$ and 3 using the CANDELS data and mapping stellar masses to halo masses

with abundance matching. At $z \sim 2$, the r_d/r_{dh} ratios obtained by Huang et al. (2017) are consistent with ours, with values of ~ 0.03 in the stellar mass range $10^9 M_\odot < M_* < 10^{10.5} M_\odot$. We note that our method is very similar to theirs. Their definitions of disk sizes and halo sizes are the same as ours. They have used four abundance matching results including that of Behroozi et al. (2013) which we also use. On the other hand, Somerville et al. (2017) have obtained somewhat higher ratios of $r_d/r_{\text{dh}} \simeq 0.4$. They have adopted a different halo definition and also taken a different method to link stellar masses to halo masses; they have carried out “forward modeling” where halos are taken from an N -body simulation and are assigned to stellar masses taking account of a random scatter. These differences may be a cause of the inconsistency in r_d/r_{dh} estimates.

To connect our study to those for low redshifts, we use Extended Press-Schechter (EPS) formalism (Bond et al. 1991; Bower 1991; Lacey & Cole 1993). The EPS formalism is able to calculate the conditional probability mass function ($f(M_2|M_1)$) of $z = z_2$ descendant halos for a given halo mass (M_1) at a high-redshift (z_1) universe by following their merger histories. We set $M_1 = 5.0 \times 10^{11} h^{-1} M_\odot$ and $z_1 = 3.0$ to follow the evolution of our halos. The lower 68 and upper percentiles of $f(M_2|M_1)$ at $z_2 = 0$ are $2.0 \times 10^{12} h^{-1} M_\odot$ and $5.6 \times 10^{12} h^{-1} M_\odot$, respectively. This implies that some fraction of our galaxies are the progenitors of objects in the Dutton & van den Bosch (2012) sample in terms of mass growth. From the results we obtain, we can depict a unified view of the angular momentum evolution. Disk galaxies maintain high j_d/m_d values during their evolution from cosmic noon to the present day, unless they lose angular momenta by some mechanisms like mergers and turn into early-type galaxies (Romanowsky & Fall 2012).

6.2.2. Halo mass dependence of j_d/m_d and the slope of the size–stellar mass relation

When we introduce the disk size–halo mass relation in Equation (11), we assume that r_d/r_{200} is constant, which means that j_*/m_* is constant irrespective of z and M_{dh} . However, it appears from Figure 8 that j_*/m_* weakly depends on both M_{dh} and z . Similar dependencies have also been shown in Huang et al. (2017) and Somerville et al. (2017): r_d/r_{dh} weakly depends on both M_{dh} and z . We approximate the observed $j_*/m_* - M_{\text{dh}}$ relation at each redshift by a power law, $j_*/m_* \propto M_{\text{dh}}^{\gamma_z}$. We find $\gamma_z = -0.09 \pm 0.02$ for $z \sim 2$, $\gamma_z = -0.13 \pm 0.01$ for $z \sim 3$, and $\gamma_z = -0.29 \pm 0.02$ for $z \sim 4$. A negative slope of $\gamma_z = -0.19 \pm 0.04$ has also been obtained by Burkert et al. (2016) for $z \sim 0.8 - 2.6$ galaxies. With a non-zero slope γ_z , Equation (11) is replaced by:

$$r_d \propto H(z)^{-2/3} M_{\text{dh}}^{\gamma_z + 1/3}. \quad (31)$$

We also approximate the stellar mass–halo mass relation by a single power-law, $M_* \propto M_{\text{dh}}^\epsilon$: $\epsilon \simeq 1.6$, from the abundance matching results of Behroozi et al. (2013). By combining these two relations, we obtain the disk size–stellar mass relation:

$$r_d \propto M_*^{1/3\epsilon + \gamma_z/\epsilon}, \quad (32)$$

$$r_d \propto M_*^{0.2 + 0.6\gamma_z}. \quad (33)$$

The slope of the size–stellar mass relation of our galaxies is $\alpha = 0.19_{-0.01}^{+0.01}$ for $z \sim 2$, $0.14_{-0.03}^{+0.01}$ for $z \sim 3$, and $0.08_{-0.05}^{+0.05}$ for $z \sim 4$ (see Section 4.2.2). The result that α is less than 0.2 for all three redshifts is explained by the negative γ_z values obtained above. We also find that the decrease in α from $z \sim 3$ to $z \sim 4$ is due to the decrease in γ_z .

Using a theoretical modified cooling model which includes disc instability, Dutton & van den Bosch (2012) have predicted a slightly negative γ_z for high redshift disk galaxies, in qualitative agreement with our results. Their negative slope reflects the fact that the mass loading factor decreases with increasing of halo mass. While this model is not consistent with their empirical model at $z \sim 0$, this model may be applicable to high redshifts. The possible decrease in γ_z from $z \sim 3$ to $z \sim 4$ found above may imply that feedback processes also change in this redshift range.

As already seen in Figure 5, van der Wel et al. (2014) have reported constant disk size–stellar mass slopes (~ 0.2) since $z \sim 2 - 0$. From the model of Equation (33), this implies that the angular momentum–halo mass relations are also flat. This is quite in agreement with the empirical results of Dutton & van den Bosch (2012) at the present-day universe. Thus Equation (33) well represents the relation between angular momentum and disk size.

6.3. Comparison with galaxy formation models

As the kinematics of galaxies provides us with important constraints on galaxy formation and evolution as well as do other global properties like stellar mass, star-formation rate, and metallicity, many modelers have attempted to reproduce the kinematic structures of galaxies. Early attempts concerning angular momentum with hydrodynamical simulations were in trouble with reproducing observations. They suffered from unexpected angular momentum loss. In those simulations, most of the angular momentum of galaxies was transferred to the background hosting halos. As a result, compact disk galaxies were produced (e.g. Navarro & Benz 1991; Navarro & White 1994). This problem is known as the “angular momentum catastrophe”.

This problem has been considerably improved by high-resolution hydrodynamical simulations with a proper treatment of feedback processes (Robertson et al. 2006; Governato et al. 2007; Scannapieco et al. 2008). In recent years, many galaxy formation simulations have succeeded in reproducing the mass–angular momentum relation for both early-type and late-type galaxies in the present-day universe (Genel et al. 2015; Teklu et al. 2015). On the other hand, at high redshifts, there do not exist theoretical studies that compare with observational data. It is still unknown that these simulations are able to reproduce the observed mass–angular momentum relation beyond $z \sim 1$. Here, we first compare our observational angular momentum results with those of some galaxy formation simulations (Sales et al. 2012; Pedrosa & Tissera 2015; Stevens et al. 2016).

In Figure 9, we compare the mass–angular momentum distribution of star-forming galaxies obtained from clustering analysis and abundance matching analysis with predictions from hydrodynamical and semi-analytical

galaxy formation models at $z \sim 2$. To directly compare with two models which give only stellar plus gas properties, we also estimate the entire disk masses by correcting for gas masses using the gas fraction estimates given in Schinnerer et al. (2016). They have investigated the gas masses for 45 massive star-forming galaxies observed with ALMA at redshifts of $z \sim 3 - 4$. We extend their results to lower mass and lower redshift by the prediction of 2-SFM (2 star formation mode) model (Sargent et al. 2014). We correct m_* and j_* by the same factor assuming that the stellar and gas disks have the same j value. The right panel of Figure 9 shows the baryonic disk mass–angular momentum relation.

Sales et al. (2012) have presented baryonic mass–angular momentum relations with various types of feedback from large cosmological N -body/gasdynamical simulations at $z \sim 2$. They have found that regardless of the strength of the feedback process m_d vs. j_d follows the same relation (the yellow solid lines in Figure 9). When strong feedbacks push out most of the baryons from the galaxies, both m_d and j_d are reduced. Pedrosa & Tissera (2015) have also analyzed the mass–angular momentum relation by decomposing disks and bulges with cosmological hydrodynamical simulations at $z \sim 0 - 2$. They have found no significant evolution since $z \sim 2$ to $z \sim 0$. The relation for total baryonic components at $z \sim 2$ is shown in Figure 9.

Stevens et al. (2016) have presented a semi-analytical model DARK SAGE, which is designed for specific understanding of angular momentum evolution. They have investigated the evolution of the stellar mass–specific angular momentum relation over $0 < z < 4.8$. The solid cyan lines in Figure 9 indicate the predicted mass–angular momentum relation at $z \sim 2$. Here, we assume the abundance matching results by Behroozi et al. (2013) to map stellar mass to dark halo mass and an analytical model by Romanowsky & Fall (2012), which connects dark matter halo mass to their halo angular momentum:

$$j_{\text{vir}} = 4.23 \times 10^4 \lambda \left(\frac{M_{\text{vir}}}{10^{12} M_{\odot}} \right)^{2/3} \text{ km s}^{-1} \text{ kpc.} \quad (34)$$

Note that as the Romanowsky & Fall (2012)’s model uses cosmological parameters at the present day ($c_{\text{vir}} = 9.7, \Delta_{\text{vir}} = 319$), we replace them with values ($c_{\text{vir}} = 4.0, \Delta_{\text{vir}} = 200$).

All of these simulations predict specific angular momenta systematically smaller than our values from both dark matter halo mass estimation methods. Our relations are almost parallel to the line of angular momentum conservation (dotted gray lines in Figure 9) regardless of mass scales, however, the simulations predict smaller specific angular momenta and the deviations are large for smaller m_* and m_d . While the star+gas plots appear to have smaller deviations than those of the star only plots, note that we ignore a possible difference in the distribution of gases and stars within galaxies. In other words, we assume that gases and stars have the same specific angular momentum. However, Brook et al. (2011) have shown that the angular momentum distributions of stars and H_I gases are different, with H_I gases having a tail of high angular momentum. Indeed, extended H_I gas disks are found in intermediate (Puech et al. 2010) and high redshift (Daddi et al. 2010) galaxies. Gases beyond

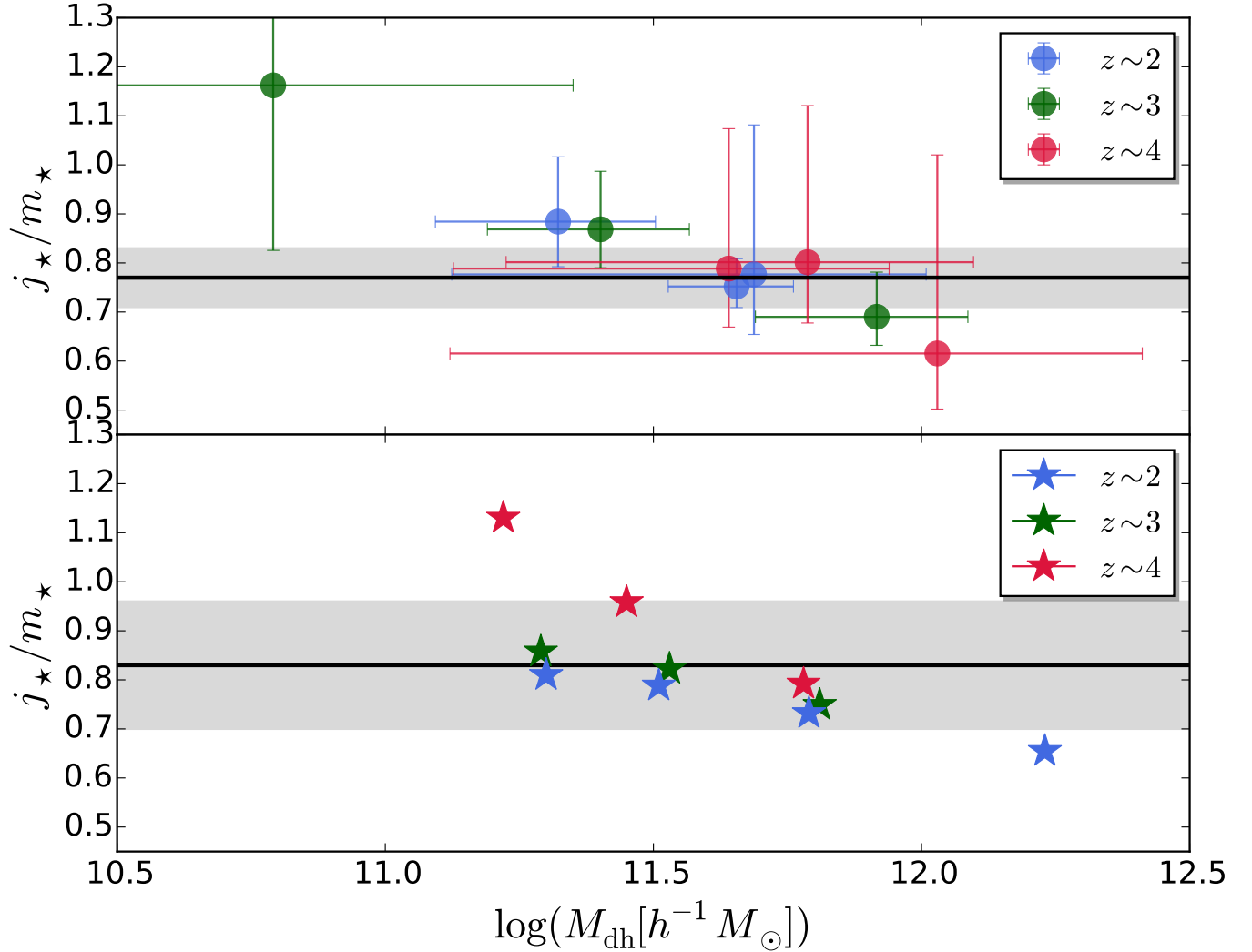


Figure 8. Angular momentum retention factor j_*/m_* vs. M_{dh} for $z \sim 2, 3$, and 4 . The colored symbols in the top panel and the bottom panel indicate the results of clustering analysis and the results of abundance matching analysis, respectively. For each panel, the black solid line and the gray shaded region indicate the average of all estimates and its 1σ error, respectively.

star-forming regions serve as a high angular momentum reservoir (Brook et al. 2011). These gases should have a larger specific angular momentum than stars. In this case, the gaps on the right panels in Figure 9 become larger.

These deviations imply that these simulations produce too small disk sizes at high redshifts. Some mechanisms that increase disk specific angular momentum at high redshifts may be needed. For example, Brook et al. (2012) have proposed that selective ejection of low angular momentum material from galaxies leads to a redistribution of angular momentum. This explains the difference in the distribution of angular momentum between dark matter halos and visible galaxies: dark matter halos have a large low angular momentum tail, while observed galaxies do not. This process reproduces large bulge-less high angular momentum galaxies.

Whether or not these feedback related mechanisms are enough to solve the deviations seen in Figure 9 is still unknown. More detailed observations and simulations are needed.

6.4. Disk instability

The angular momentum of disks is also closely related to their global instabilities. Disks can be unstable against bar mode instability, because low angular momentum material forms a bar (Shen et al. 2003). Efstathiou et al. (1982) have investigated this kind of instabilities for an exponential disk embedded in a variety of halos using N -body simulations and found a stellar disk is globally unstable against bar formation under the criterion:

$$\epsilon_m \equiv \frac{V_{\text{max}}}{(GM_d/r_d)^{1/2}} \lesssim 1.1, \quad (35)$$

where V_{max} is the maximum rotation velocity of the disk. The threshold for gaseous disks is $\epsilon_m \simeq 0.9$. According to Mo et al. (1998), for a NFW halo, this criterion is well approximated by

$$\lambda' < m_d, \quad (36)$$

where $\lambda' \equiv \lambda j_d/m_d$.

We note that the criteria of Equations (35) and (36) are not strict. Guo et al. (2011) have proposed an alternative

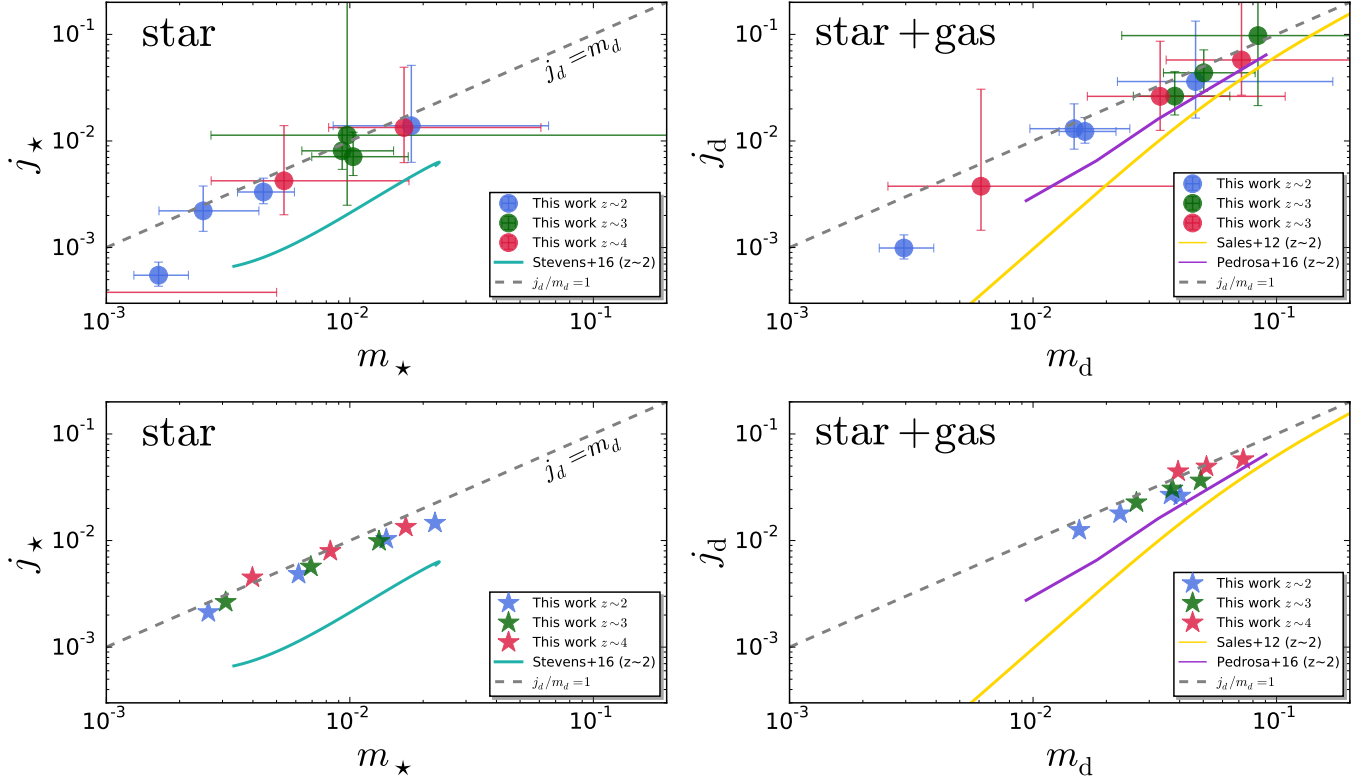


Figure 9. Observed mass–angular momentum relation compared with three hydrodynamical and semi-analytic galaxy formation simulations. The left panels show the relation for the stellar component and the right panels for the stellar plus gas component. The colored symbols in the top panels are the results obtained from clustering analysis and those in the bottom panels are from abundance matching analysis. The solid cyan lines on the left panels indicate the semi-analytical galaxy formation simulation of [Stevens et al. \(2016\)](#) at $z \sim 2$. The solid purple and yellow lines on the right panels indicate the hydrodynamical galaxy formation simulations of [Sales et al. \(2012\)](#) and [Pedrosa & Tissera \(2015\)](#), respectively, at $z \sim 2$. The gray dashed lines indicate the line of angular momentum conservation.

criterion, $V_{\max} < \sqrt{GM_d/3r_d}$, which reflects that V_{\max} of the real dark matter halo systems is smaller than that of ideal systems. In this paper, we use Equation (36).

We show in Figure 10 the distribution in the $\lambda' - m_d$ plane of our star-forming galaxies over $z \sim 2 - 4$. We find most of the data points to be near the line of instability over the entire redshift range regardless of the method to estimate dark halo masses. This implies some fractions of $z \sim 2 - 4$ galaxies may be dynamically changing the disk structure toward forming a bar and a bulge through bar formation.

To compare with local spiral galaxies, we assume $\lambda = 0.04$ and $j_d/m_d \simeq 0.6$ ([Romanowsky & Fall 2012](#)) in the present-day Universe. Then, the average value of λ' is estimated as 0.024. The abundance matching result of [Behroozi et al. \(2013\)](#) predicts m_d lower than 0.024 in a wide range of halo mass. This displays that local spiral galaxies appear to be more stable than high redshift galaxies.

We have to keep in mind again that we should take into account a possible difference in angular momentum between gases and stars mentioned in Section 6.3. In this case, the plots in Figure 10 will move to more stable regions.

Other than the global instability, there exist scenarios that form bars and bulges ([Mo et al. 2010](#)). For example, an interaction with a massive perturber leads to a bar-like structure ([Noguchi 1987](#)). In addition to this, the migration of giant clumps, which are created

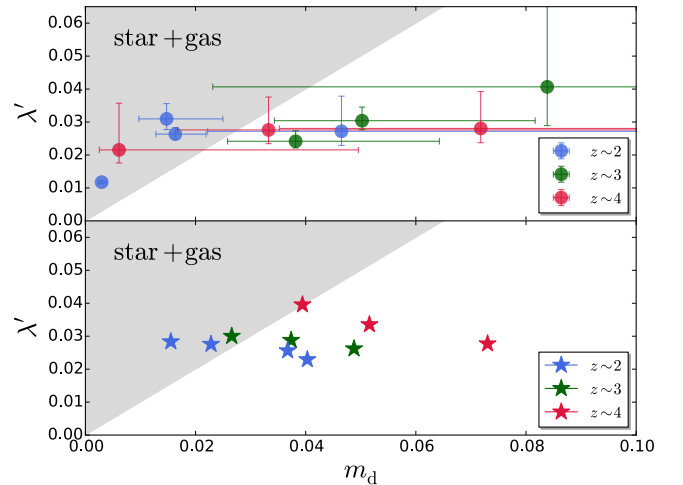


Figure 10. Diagram of λ' vs. m_d at $z \sim 2, 3$, and 4. The colored symbols in the top panel and the bottom panel indicate results from clustering analysis and abundance matching analysis, respectively. Galaxies in the gray shaded regions are unstable against bar-mode instability.

by local Toomre Q instabilities ([Toomre 1964](#)), grows a bulge. Global instability may be one of the ways to explain galaxies with bars or bulges in the local Universe.

7. CONCLUSION

In this paper, we have used the 3D-HST GOODS-South, COSMOS, and AEGIS imaging data and galaxy catalog to analyze the relation between the ratio of the disk stellar mass to the halo mass, $m_* \equiv M_*/M_{\text{dh}}$, and the fraction of the dark halo angular momentum transferred to the stellar disk, $j_* \equiv J_*/J_{\text{dh}}$ for 11738 star-forming galaxies over the stellar mass range $8.3 < \log(M_*/M_\odot) < 11.1$ at $z \sim 2, 3$, and 4. For each redshift, we have divided the catalog into several M_* bins and infer M_{dh} by two independent methods, clustering analysis and abundance matching, to obtain an average m_* value for each bin. We have confirmed that the two mass estimators give consistent results. For our objects we have also measured effective radii r_{d} at rest 5000Å with GALFIT, and combined them with m_* and M_{dh} estimates to obtain j_* by applying Mo et al. (1998) analytic model of disk formation. The followings are the main results of this paper.

(i) We have found the median size evolution of disk star-forming galaxies $\bar{r}_{\text{d}}(M_{*,10})/\text{kpc} = 6.88(1+z)^{-0.91 \pm 0.01}$ at $M_* = 1.0 \times 10^{10} M_\odot$. This redshift evolution is in agreement with the results by Allen et al. (2016) and Shibuya et al. (2015). We have also analyzed the slope of the disk size–stellar mass relation. While the slope is consistent with the results by van der Wel et al. (2014) at $z \sim 2$, we have found that the slope becomes shallower beyond $z \sim 2$. The scatter of $r_{\text{d}}-M_*$ relation is $\sigma_{\ln r_{\text{d}}} \sim 0.4 - 0.6$ over the redshift range examined, which is comparable with the scatter of the log-normal distribution of λ .

(ii) We have obtained the angular momentum retention factor j_*/m_* averaged over mass and redshift to be $\simeq 0.77 \pm 0.06$ from clustering analysis and $\simeq 0.83 \pm 0.13$ from abundance matching. These values are in rough agreement with those of local late-type galaxies by Romanowsky & Fall (2012) and those of star-forming galaxies at $z \sim 0.8 - 2.6$ by Burkert et al. (2016).

(iii) Contrary to the star-forming galaxies at the present-day universe, j_*/m_* appears to decrease with halo mass especially when abundance matching is used as the mass estimator. Combined with the slope of the M_*-M_{dh} relation, this negative slope of the j_*/m_*-M_{dh} relation explains the shallow (< 0.2) slopes of the $r_{\text{d}}-M_*$ relation obtained in this paper. We have also found a possible decrease in the j_*/m_*-M_{dh} slope from $z \sim 2$ to $z \sim 4$, which may imply that feedback processes also change over this redshift range.

(iv) We have for the first time compared the observed mass–angular momentum relation with those of the recent galaxy formation simulations at $z \sim 2$ by Sales et al. (2012), Pedrosa & Tissera (2015), and Stevens et al. (2016). We have found that all of these simulations predict specific angular momenta systematically smaller than our values, which implies that these simulations produce too small disks at high redshifts while reproducing local measurements. We have also found that a significant fraction of our galaxies appear to be unstable against bar formation.

ACKNOWLEDGMENTS

This work is based on observations taken by the 3D-HST Treasury Program (GO 12177 and 12328) with the NASA/ESA HST, which is operated by the Association of Universities for Research in Astronomy, Inc., under NASA contract NAS5-26555. This work is supported by KAKENHI (16K05286) Grant-in-Aid for Scientific Research (C) through Japan Society for the Promotion of Science (JSPS). R.K. acknowledges support from Grant-in-Aid for JSPS Research Fellow (16J01302).

REFERENCES

- Allen, R. J., Kacprzak, G. G., Glazebrook, K., et al. 2016, ArXiv e-prints, arXiv:1612.05262
- Bardeen, J. M., Bond, J. R., Kaiser, N., & Szalay, A. S. 1986, ApJ, 304, 15
- Barnes, J., & Efstathiou, G. 1987, ApJ, 319, 575
- Barone-Nugent, R. L., Trenti, M., Wyithe, J. S. B., et al. 2014, ApJ, 793, 17
- Behroozi, P. S., Wechsler, R. H., & Conroy, C. 2013, ApJ, 770, 57
- Bertin, E., & Arnouts, S. 1996, A&AS, 117, 393
- Bond, J. R., Cole, S., Efstathiou, G., & Kaiser, N. 1991, ApJ, 379, 440
- Bower, R. G. 1991, MNRAS, 248, 332
- Brammer, G. B., van Dokkum, P. G., & Coppi, P. 2008, ApJ, 686, 1503
- Brammer, G. B., van Dokkum, P. G., Franx, M., et al. 2012, ApJS, 200, 13
- Brennan, R., Pandya, V., Somerville, R. S., et al. 2017, MNRAS, 465, 619
- Brook, C. B., Stinson, G., Gibson, B. K., et al. 2012, MNRAS, 419, 771
- Brook, C. B., Governato, F., Roškar, R., et al. 2011, MNRAS, 415, 1051
- Bullock, J. S., Dekel, A., Kolatt, T. S., et al. 2001, ApJ, 555, 240
- Burkert, A., Förster Schreiber, N. M., Genzel, R., et al. 2016, ApJ, 826, 214
- Carroll, S. M., Press, W. H., & Turner, E. L. 1992, ARA&A, 30, 499
- Chabrier, G. 2003, PASP, 115, 763
- Ciotti, L., & Bertin, G. 1999, A&A, 352, 447
- Colín, P., Avila-Reese, V., Roca-Fàbrega, S., & Valenzuela, O. 2016, ApJ, 829, 98
- Contini, T., Epinat, B., Bouché, N., et al. 2016, A&A, 591, A49
- Courteau, S., Dutton, A. A., van den Bosch, F. C., et al. 2007, ApJ, 671, 203
- Croton, D. J., Stevens, A. R. H., Tonini, C., et al. 2016, ApJS, 222, 22
- Daddi, E., Bournaud, F., Walter, F., et al. 2010, ApJ, 713, 686
- Davis, A. J., & Natarajan, P. 2009, MNRAS, 393, 1498
- Dutton, A. A., Conroy, C., van den Bosch, F. C., Prada, F., & More, S. 2010, MNRAS, 407, 2
- Dutton, A. A., & van den Bosch, F. C. 2012, MNRAS, 421, 608
- Dutton, A. A., Conroy, C., van den Bosch, F. C., et al. 2011, MNRAS, 416, 322
- Efstathiou, G., Bernstein, G., Tyson, J. A., Katz, N., & Guhathakurta, P. 1991, ApJL, 380, L47
- Efstathiou, G., Lake, G., & Negroponte, J. 1982, MNRAS, 199, 1069
- Fall, S. M. 1983, in IAU Symposium, Vol. 100, Internal Kinematics and Dynamics of Galaxies, ed. E. Athanassoula, 391–398
- Fall, S. M., & Efstathiou, G. 1980, MNRAS, 193, 189
- Fall, S. M., & Romanowsky, A. J. 2013, ApJL, 769, L26
- Ferguson, H. C., Dickinson, M., Giavalisco, M., et al. 2004, ApJL, 600, L107
- Foreman-Mackey, D. 2016, The Journal of Open Source Software, 24, doi:10.21105/joss.00024
- Foreman-Mackey, D., Hogg, D. W., Lang, D., & Goodman, J. 2013, PASP, 125, 306
- Foucaud, S., Conselice, C. J., Hartley, W. G., et al. 2010, MNRAS, 406, 147
- Foucaud, S., McCracken, H. J., Le Fèvre, O., et al. 2003, A&A, 409, 835
- Genel, S., Fall, S. M., Hernquist, L., et al. 2015, ApJL, 804, L40
- Governato, F., Willman, B., Mayer, L., et al. 2007, MNRAS, 374, 1479
- Grogin, N. A., Kocevski, D. D., Faber, S. M., et al. 2011, ApJS, 197, 35
- Groth, E. J., & Peebles, P. J. E. 1977, ApJ, 217, 385
- Guo, Q., White, S., Boylan-Kolchin, M., et al. 2011, MNRAS, 413, 101

- Harikane, Y., Ouchi, M., Ono, Y., et al. 2016, *ApJ*, 821, 123
Huang, K.-H., Ferguson, H. C., Ravindranath, S., & Su, J. 2013, *ApJ*, 765, 68
Huang, K.-H., Fall, S. M., Ferguson, H. C., et al. 2017, *ApJ*, 838, 6
Kawamata, R., Ishigaki, M., Shimasaku, K., Oguri, M., & Ouchi, M. 2015, *ApJ*, 804, 103
Koekemoer, A. M., Faber, S. M., Ferguson, H. C., et al. 2011, *ApJS*, 197, 36
Kravtsov, A. V. 2013, *ApJL*, 764, L31
Kriek, M., van Dokkum, P. G., Labbé, I., et al. 2009, *ApJ*, 700, 221
Lacey, C., & Cole, S. 1993, *MNRAS*, 262, 627
Landy, S. D., & Szalay, A. S. 1993, *ApJ*, 412, 64
Lee, K.-S., Giavalisco, M., Gnedin, O. Y., et al. 2006, *ApJ*, 642, 63
MacArthur, L. A., Courteau, S., & Holtzman, J. A. 2003, *ApJ*, 582, 689
Mo, H., van den Bosch, F. C., & White, S. 2010, *Galaxy Formation and Evolution*
Mo, H. J., Mao, S., & White, S. D. M. 1998, *MNRAS*, 295, 319
Navarro, J. F., & Benz, W. 1991, *ApJ*, 380, 320
Navarro, J. F., & White, S. D. M. 1994, *MNRAS*, 267, 401
Noguchi, M. 1987, *MNRAS*, 228, 635
Oke, J. B., & Gunn, J. E. 1983, *ApJ*, 266, 713
Ouchi, M., Shimasaku, K., Okamura, S., et al. 2001, *ApJL*, 558, L83
—, 2004, *ApJ*, 611, 685
Ouchi, M., Shimasaku, K., Furusawa, H., et al. 2010, *ApJ*, 723, 869
Pedrosa, S. E., & Tissera, P. B. 2015, *A&A*, 584, A43
Peebles, P. J. E. 1969, *ApJ*, 155, 393
—, 1975, *ApJ*, 196, 647
—, 1980, *The large-scale structure of the universe*
Peng, C. Y., Ho, L. C., Impey, C. D., & Rix, H.-W. 2002, *AJ*, 124, 266
—, 2010, *AJ*, 139, 2097
Porter, L. A., Somerville, R. S., Primack, J. R., & Johansson, P. H. 2014, *MNRAS*, 444, 942
Prada, F., Klypin, A. A., Cuesta, A. J., Betancort-Rijo, J. E., & Primack, J. 2012, *MNRAS*, 423, 3018
Puech, M., Hammer, F., Flores, H., et al. 2010, *A&A*, 510, A68
Robertson, B., Bullock, J. S., Cox, T. J., et al. 2006, *ApJ*, 645, 986
Roche, N., & Eales, S. A. 1999, *MNRAS*, 307, 111
Rodríguez-Puebla, A., Behroozi, P., Primack, J., et al. 2016, *MNRAS*, 462, 893
Romanowsky, A. J., & Fall, S. M. 2012, *ApJS*, 203, 17
Sales, L. V., Navarro, J. F., Theuns, T., et al. 2012, *MNRAS*, 423, 1544
Salpeter, E. E. 1955, *ApJ*, 121, 161
Sargent, M. T., Daddi, E., Béthermin, M., et al. 2014, *ApJ*, 793, 19
Scannapieco, C., Tissera, P. B., White, S. D. M., & Springel, V. 2008, *MNRAS*, 389, 1137
Schinnerer, E., Groves, B., Sargent, M. T., et al. 2016, *ApJ*, 833, 112
Shen, S., Mo, H. J., White, S. D. M., et al. 2003, *MNRAS*, 343, 978
Sheth, R. K., Mo, H. J., & Tormen, G. 2001, *MNRAS*, 323, 1
Shibuya, T., Ouchi, M., & Harikane, Y. 2015, *ApJS*, 219, 15
Skelton, R. E., Whitaker, K. E., Momcheva, I. G., et al. 2014, *ApJS*, 214, 24
Smith, R. E., Peacock, J. A., Jenkins, A., et al. 2003, *MNRAS*, 341, 1311
Somerville, R. S., Hopkins, P. F., Cox, T. J., Robertson, B. E., & Hernquist, L. 2008, *MNRAS*, 391, 481
Somerville, R. S., Behroozi, P., Pandya, V., et al. 2017, *ArXiv e-prints*, arXiv:1701.03526
Steinmetz, M., & Navarro, J. F. 1999, *ApJ*, 513, 555
Stevens, A. R. H., Croton, D. J., & Mutch, S. J. 2016, *MNRAS*, 461, 859
Teklu, A. F., Remus, R.-S., Dolag, K., et al. 2015, *ApJ*, 812, 29
Toomre, A. 1964, *ApJ*, 139, 1217
van der Wel, A., Franx, M., van Dokkum, P. G., et al. 2014, *ApJ*, 788, 28
Vitvitska, M., Klypin, A. A., Kravtsov, A. V., et al. 2002, *ApJ*, 581, 799
White, S. D. M., & Frenk, C. S. 1991, *ApJ*, 379, 52
Zhu, C., Byrd, R. H., Lu, P., & Nocedal, J. 1997, *ACM Trans. Math. Softw.*, 23, 550

APPENDIX

Before clustering analysis in Section 5, we calculate the angular correlation functions for all five fields. We separate each sample to luminosity bins, and compare with previous results (Ouchi et al. 2004; Lee et al. 2006; Barone-Nugent et al. 2014). Figure 11 shows the angular correlation functions for the GOODS-North and UDS fields. The clustering properties for these two fields are relatively smaller than the values by the previous results. The GOODS-North field has a negative correlation with luminosity. The UDS field has a smaller angular correlation function and there are no signals beyond 100 arcsec. Because of this strange behavior, we does not include these two fields for our analysis. The cause of this weak clustering properties is not clear. The small number of filters used for SED fitting may affect clustering properties.

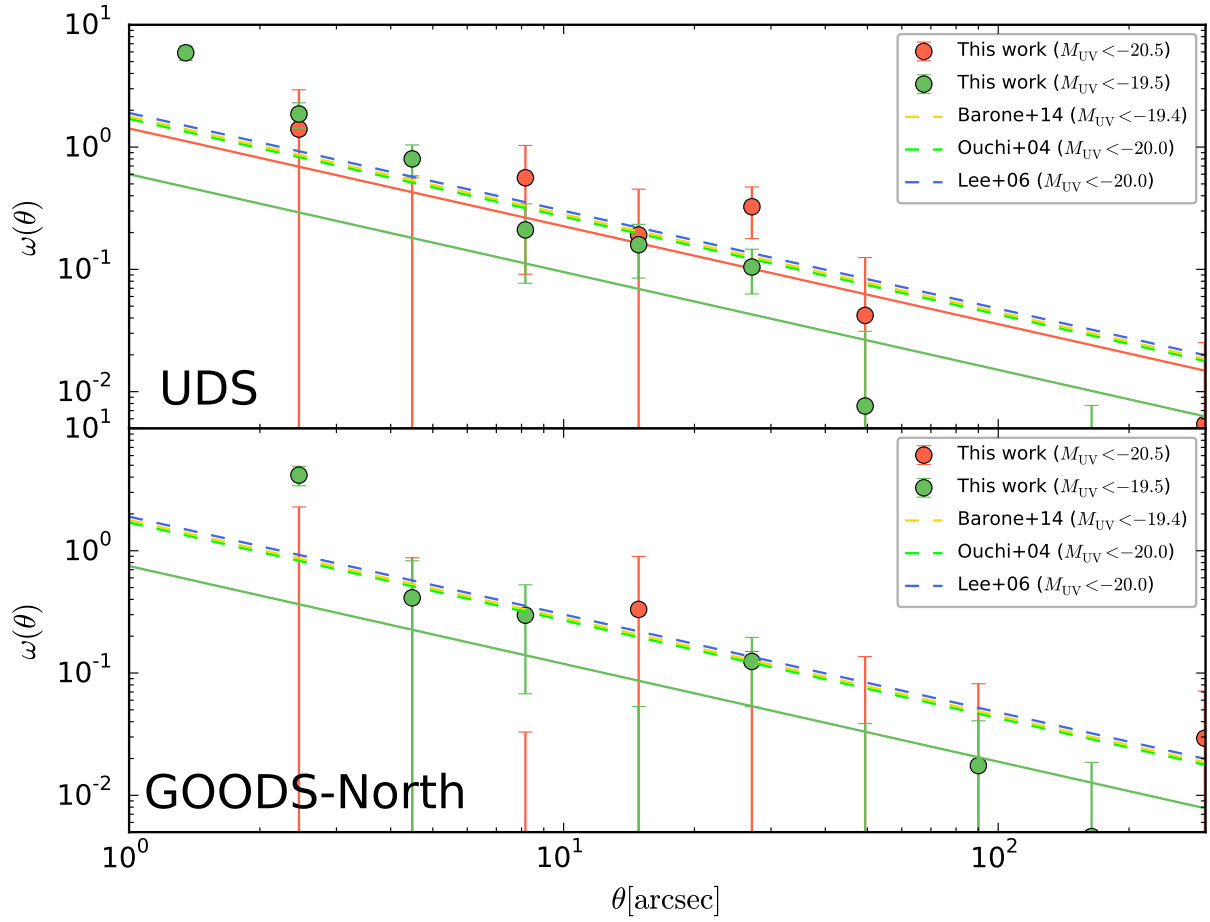


Figure 11. Angular correlation functions in the UDS (top panel) and GOODS-North (bottom) at $z \sim 4$ compared with three previous results. The solid red and green lines indicate the best-fit power laws for luminosity bins. The dashed yellow, green, and blue lines indicate the results by Barone-Nugent et al. (2014), Ouchi et al. (2004), and Lee et al. (2006), respectively.